Thermocapillary instabilities in a laterally heated liquid bridge with end wall rotation

L. Kahouadji,[1] B. C. Houchens,[2] and L. Martin Witkowski[1,a)]
[1]*CNRS, UPR 3251, LIMSI, F-91403, Orsay, France and UPMC, 4 place Jussieu, F-75005, Paris, France*
[2]*Department of Mechanical Engineering and Materials Science, Rice University, Houston, Texas 77005, USA*

(Received 11 April 2011; accepted 31 August 2011; published online 24 October 2011)

The effect of rotation on the stability of thermocapillary driven flow in a laterally heated liquid bridge is studied numerically using the full-zone model of the floating-zone crystal growth technique. A small Prandtl number (0.02) fluid, relevant for semiconductor melts, is studied with an aspect ratio (height to diameter of the melt) equal to one. Buoyancy is neglected. A linear stability analysis of three-dimensional perturbations is performed and shows that for any ratio of angular velocities, a weak rotation rate has the surprising effect of destabilizing the base flow. By systematically varying the rotation rate and ratio of angular velocities, the critical threshold and azimuthal wave number of the most unstable mode is found over a wide range of this two parameter space. Depending on these parameters, the leading eigenmode is a wave propagating either in the positive or negative azimuthal direction, with kinetic energy typically localized close to one of the end walls. These results are of practical interest for industrial crystal growth applications, where rotation is often used to obtain higher quality crystals. © *2011 American Institute of Physics*. [doi:10.1063/1.3644717]

I. INTRODUCTION

Optimizing bulk production of high-quality crystals for semiconductor devices is still an issue in the electronics industry. Many bulk melt processes exist. One of them, the radio-frequency heated, single coil float-zone is represented in Fig. 1 (left). This technique has been used to grow small diameter crystal for instance by Dold.[1] As the technique is containerless, few impurities are introduced into the crystal and the stresses during cooling are reduced so that high-purity, dislocation-free crystals are obtained. A complete description of this technique can be found in Refs. 2 and 3 and here the focus is only on the main difficulties that crystal growers face when using this process. For a doped silicon single crystal, large-scale, non-uniform distribution of dopants (macro-segregation) results from large-scale flow in the molten zone and small scale distribution (striations or micro-segregation) is a consequence of time-dependent flow at the solidification front. Macro-segregation and striations need to be controlled to obtain uniform distribution of dopants, and rotation is an effective way to modify the flow structure and provide this control.

For large-diameter crystals grown by float-zone the heat source is provided by a high-frequency inductor. As semiconductor melts, such as molten silicon, are good electrical conductors, the alternating magnetic flux induces electric current in the molten zone and Joulean dissipation provides the necessary heat source to maintain the material above the melting temperature. Unfortunately, as electric current is supplied to the inductor ring with two wires, heating and electromagnetic body forces are not uniform in the azimuthal direction.[4] Rotation of the heater is technically difficult to achieve so the most common situation is to rotate the feed rod, the crystal or both to minimize the impact of this deleterious asymmetry.

Up to centimeter-scale diameter crystals can be grown by optically heated float-zone using an ellipsoidal mirror furnace.[5] This is an efficient and again containerless technique to melt the polycrystalline feed rod, but as the diameter increases the heat flux provided by radiation from the optical source becomes insufficient. Again, the negative impact of small nonuniformities in the heat flux can be offset by rotation.

In order to explain the basic effects of rotation on the flow driven by thermocapillary convection, a simplified model represented in Fig. 1 (right) is investigated. The molten zone is held between the feed rod and the crystal by surface tension. Both melting and solidification fronts are assumed to be flat disks. The free surface is assumed to have a cylindrical shape of constant radius. Deformation from gravity and centrifugal acceleration due to rotation is neglected. A simple analytical expression is selected for the distribution of heat flux along the free surface. This model has already been proposed several times[6–8] and is sometimes referred to as the full-zone. The parabolic expression for the heat flux is that used in Ref. 8. Different heat flux distributions have also been studied in Ref. 9. The specific heat flux distribution is important for strong thermocapillary flow. However, Gelfgat *et al.*[10] showed that the primary bifurcation that occurs for moderate convective flow depends simply on the total amount of heat flux provided. Note that the full-zone is an idealization of crystal growth and does not account for the heat of fusion at the melt and solidfication fronts. In reality, these effects would break the midplane reflection symmetry of the thermal field and, hence, the flow field, in the melt.

Even if the interfaces are not solidifying and melting, the full-zone model is not easy to realize experimentally as the heat flux is difficult to monitor precisely. Therefore,

a)Electronic mail: witko@limsi.fr.

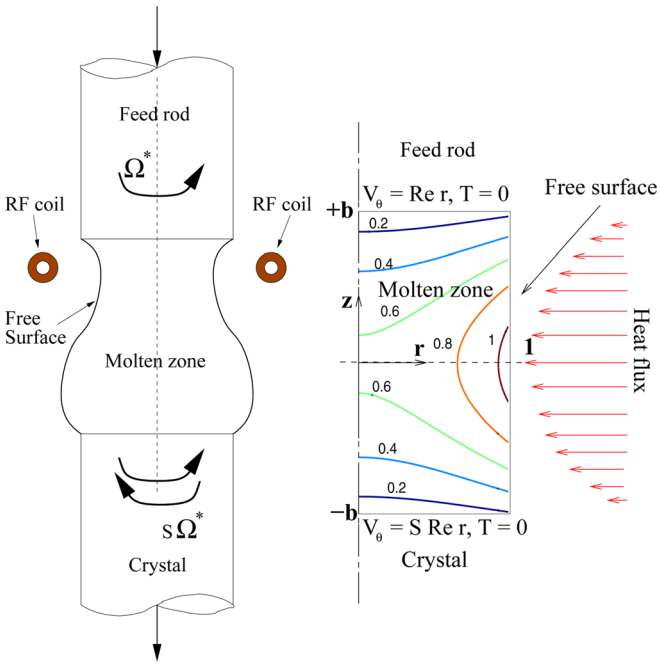

FIG. 1. (Color online) Left: Schema of the radio-frequency (RF) heated float-zone process. Right: academic model for $b = 1$ and the temperature distribution neglecting convection ($\mathrm{Ma} = 0$ and $\mathrm{Re} = 0$).

another model called the half-zone, which aims to represent half of the floating-zone process, has been widely studied by experimentalists.[11,12] A thorough review of half-zone and full-zone experimental studies in microgravity is given by Kawamura *et al.*[13] In the half-zone, the temperature gradient along the free surface is a consequence of the temperature difference imposed on the disks. This configuration stimulated many numerical studies (see Ref. 14 for a complete review). Nevertheless, numerical investigation of the full-zone stability has again become popular because it allows perturbations that break the reflection symmetry of the base flow with respect to the midplane.[10,15,16] A comparison between the half-zone and full-zone has been carried out in Ref. 17 and shows that the dominant mechanism for the leading instability is qualitatively captured by the half-zone for Prandtl numbers less than 0.05. This justifies most of the studies on the half-zone configuration, at least to the first instability. However, if rotation is involved the half-zone model is of questionable value. When the crystal and the feed rod rotate at different angular velocities, the midplane reflection symmetry assumed in the half-zone no longer holds.

Experimental studies of heated liquid bridges involving rotation are scarce. An isothermal study was carried out by Carruthers and Grasso,[18] but the shear induced by the fluid surrounding the liquid bridge strongly affected the flow. In fact, the case of isorotation of the upper and lower disks presented in their figure 7 indicates a deviation from uniform solid body rotation. Chun *et al.*[19,20] studied both the full-zone and half-zone with rotation. More quantitative results are found in the latter paper which focuses only on the half-zone with isorotation of both disks or single rotation of one disk. In both studies, the heat flux or temperature difference was such that the flow was beyond the onset of oscillatory flow: namely a traveling wave in the azimuthal direction. It was shown that for a large enough angular velocity, rotation reduced the amplitude of oscillations. For the half-zone and rotation of the cold disk, Kamotani and Kim[21] gave a detailed study on the onset of oscillations as a function of rotation rate. It was observed that a weak rotation rate is destabilizing. In all of these experiments, large Prandtl number fluids were used. For small Prandtl number fluids, quantitative information about the flow is extremely difficult to obtain experimentally. The most common method to collect experimental data to relate to the bulk flow is to introduce a dopant in the melt and analyze the resulting dopant distribution in the grown crystal. This provides some indirect indication of the fluid flow at the solidification front.[3]

The pioneering numerical analysis by Chang and Wilcox[22] that describes the thermocapillary flow in the liquid bridge was then extended by Kobayashi *et al.*[6,23] to include the effect of rotation. An earlier isothermal attempt by Chang[24] led to unreliable results due to an erroneous boundary condition for the azimuthal velocity. These studies focus on the flow beyond the first bifurcation. To the authors' knowledge, the first numerical stability analysis of the flow in a liquid bridge with rotation was performed by Harriot and Brown.[25] This study was restricted to isothermal flow, exact (or nearly exact) counter-rotating disks and axisymmetric perturbations. The quality of the results is remarkable given the computational facilities of the time. Unfortunately, for an aspect ratio of interest for crystal growth, the critical value of rotation rate is too large for accurate predictions with the limited resolution.

Utilizing the electrical properties of molten semiconductors, an alternative control method that provides angular momentum to the flow is the application of a rotating magnetic field, which produces, under certain conditions, a purely azimuthal body force. The linear stability analysis of the flow in a laterally heated bridge with a rotating magnetic field was carried out by Walker *et al.*[26] and Ma *et al.*[27] The latter work combines isorotation of the disks and the rotating magnetic field. The effect of the rotating magnetic field is very similar to the effect of isorotation of the disks, as discussed in Ref. 26. A weak rotation destabilizes the flow as observed in Ref. 21. The destabilization of a Marangoni (or buoyant) flow by weak rotation has also been observed in different crystal growth configurations, namely the Czochralski technique, for both small and large Prandtl number fluids.[28–30]

To complete this short survey, Minakuchi *et al.*[31] seems the only study to have performed a three-dimensional simulation corresponding to the full-zone with rotation. In the exact counter-rotating configuration, it was shown qualitatively that the oscillatory thermocapillary flow is stabilized by rotation for three rotation rates, a small Prandtl number fluid and a short aspect ratio such that the distance between the feed rod and the crystal is equal to the radius. These numerical simulations also include solute transport as a passive scalar and are performed with moderate numerical resolution that is slightly under-resolved for the high-rotation rate.

The purpose of the present article is to provide an understanding of the influence of rotation, for any angular velocity ratio of the disks, on the stability of the flow driven by Marangoni convection in a laterally heated liquid bridge.

II. PROBLEM FORMULATION, GOVERNING EQUATIONS, AND NUMERICAL METHOD

The model geometry is represented in Fig. 1 (right). Cylindrical coordinates (r^*, θ, z^*) are used, where asterisks indicate dimensional variables. The free surface is located at a constant radius R^* and thus is assumed to be nondeformable. In experiments, even in microgravity, the free surface will deform. In microgravity and with no rotation, this deformation is symmetric with respect to the midplane. However, differential rotation or any gravitational field will break the midplane reflection symmetry of the domain. The distance between the feed rod and the crystal is $2bR^*$ where b is the aspect ratio. The fluid is Newtonian with constant physical properties with the exception of the surface tension γ^* which is assumed to vary linearly with temperature T^* given by

$$\gamma^*(T^*) = \gamma^*(T_S^*) + \frac{\mathrm{d}\gamma^*}{\mathrm{d}T^*}(T^* - T_S^*), \tag{1}$$

where T_S^* is the solidification temperature. The coefficient $\frac{\mathrm{d}\gamma^*}{\mathrm{d}T^*}$ is typically negative for the liquid-gas interface of interest for crystal growth. The melting and solidification front are perpendicular to the revolution axis and rotate at angular velocities Ω^* and $\mathrm{S}\Omega^*$, respectively, where S the angular velocity ratio between the feed rod and the crystal. The characteristic scaling selected for the velocity V^* is $V^* = \nu^*/R^*$, where ν^* is the kinematic viscosity. Length, time, and pressure are scaled by R^*, R^*/V^*, and $\rho^* V^{*2}$, respectively, where ρ^* is the density of the melt. The difference $T^* - T_S^*$ between the melt and the solidification temperature is scaled as $T = \left(T^* - T_S^*\right)/\Delta T^*$, where the characteristic temperature difference $\Delta T^* = q^* R^*/k^*$ is based on the maximum q^* of the heat flux,

$$k^* \frac{\partial T^*}{\partial r^*} = q^* \left(1 - \left(\frac{z^*}{bR^*}\right)^2\right) \tag{2}$$

prescribed along the free surface. Here k^* denotes the thermal conductivity.

The nondimensional continuity, Navier-Stokes and energy equations, neglecting buoyancy, are

$$\nabla \cdot \mathbf{v} = 0, \tag{3}$$

$$\frac{\partial \mathbf{v}}{\partial t} + (\mathbf{v} \cdot \nabla)\mathbf{v} = -\nabla P + \nabla^2 \mathbf{v}, \tag{4}$$

$$\frac{\partial T}{\partial t} + (\mathbf{v} \cdot \nabla)T = \frac{1}{\mathrm{Pr}} \nabla^2 T. \tag{5}$$

The boundary conditions at the free surface $r = 1$ are

$$V_r = 0, \tag{6}$$

$$\frac{\partial V_\theta}{\partial r} - \frac{V_\theta}{r} = -\frac{\mathrm{Ma}}{\mathrm{Pr}} f_z \frac{1}{r} \frac{\partial T}{\partial \theta}, \tag{7}$$

$$\frac{\partial V_z}{\partial r} = -\frac{\mathrm{Ma}}{\mathrm{Pr}} f_z \frac{\partial T}{\partial z}, \tag{8}$$

$$\frac{\partial T}{\partial r} = 1 - \left(\frac{z}{b}\right)^2, \tag{9}$$

and at the solid-liquid interfaces

$$V_r = 0, \quad V_\theta = \mathrm{Re}\, r, \quad V_z = 0, \quad T = 0 \quad \text{at } z = b, \tag{10}$$

$$V_r = 0, \quad V_\theta = \mathrm{S}\,\mathrm{Re}\, r, \quad V_z = 0, \quad T = 0 \quad \text{at } z = -b. \tag{11}$$

The nondimensional Marangoni, Prandtl and Reynolds numbers are defined by

$$\mathrm{Ma} = \frac{-\frac{\mathrm{d}\gamma^*}{\mathrm{d}T^*} q^* R^{*2}}{\rho^* \nu^* \kappa^* k^*}, \quad \mathrm{Pr} = \frac{\nu^*}{\kappa^*} \text{ and } \mathrm{Re} = \frac{\Omega^* R^{*2}}{\nu^*}, \tag{12}$$

respectively, and where κ^* is the thermal diffusivity. The singularity at the corner $r = 1$ and $z = \pm b$ is removed with a regularization function $f_z = 1 - \exp(-\alpha(1 - (z/b)^2)^2)$ where α is the regularization parameter. Here $\alpha = 200$ is fixed, which seems to be a reasonable value.[17] Similar regularization procedures have often been used and are widely discussed.[7,17,32–35]

A. Base flow

The base flow, before the first bifurcation, is stationary and axisymmetric. The scalar functions for vorticity $\omega^b(r, z)$ and the stream function $\psi^b(r, z)$ are introduced. These are related to the meridional velocity field V_r^b and V_z^b by

$$\omega^b = \frac{\partial V_r^b}{\partial z} - \frac{\partial V_z^b}{\partial r}, \tag{13}$$

$$V_r^b = \frac{1}{r}\frac{\partial \psi^b}{\partial z} \quad \text{and} \quad V_z^b = -\frac{1}{r}\frac{\partial \psi^b}{\partial r}. \tag{14}$$

The equations, discretization, and the resolution technique are almost identical to those presented in the context of a rotating magnetic field applied to the floating-zone configuration.[36] The difference is that the flow in the azimuthal direction is here driven by the imposed liquid-solid interface rotation, rather than by an azimuthal body force created by the rotating magnetic field. In general, there is no symmetry in z as the angular velocity ratio S is varied over the range $[-1, 1]$. For the base flow, the Navier-Stokes equations reduce to

$$\frac{\partial (V_r^b \omega^b)}{\partial r} + \frac{\partial (V_z^b \omega^b)}{\partial z} - \frac{\partial}{\partial z}\left(\frac{V_\theta^{b2}}{r}\right) = \frac{\partial^2 \omega^b}{\partial r^2} + \frac{1}{r}\frac{\partial \omega^b}{\partial r} - \frac{\omega^b}{r^2} + \frac{\partial^2 \omega^b}{\partial z^2}, \tag{15}$$

$$\frac{\partial^2 \psi^b}{\partial r^2} - \frac{1}{r}\frac{\partial \psi^b}{\partial r} + \frac{\partial^2 \psi^b}{\partial z^2} = r\omega^b, \tag{16}$$

$$\frac{\partial (V_r^b V_\theta^b)}{\partial r} + \frac{2 V_r^b V_\theta^b}{r} + \frac{\partial (V_z^b V_\theta^b)}{\partial z} = \frac{\partial^2 V_\theta^b}{\partial r^2} + \frac{1}{r}\frac{\partial V_\theta^b}{\partial r} - \frac{V_\theta^b}{r^2} + \frac{\partial^2 V_\theta^b}{\partial z^2}. \tag{17}$$

The energy equation is

$$\frac{\partial (V_r^b T^b)}{\partial r} + \frac{V_r^b T^b}{r} + \frac{\partial (V_z^b T^b)}{\partial z} = \frac{1}{\mathrm{Pr}}\left(\frac{\partial^2 T^b}{\partial r^2} + \frac{1}{r}\frac{\partial T^b}{\partial r} + \frac{\partial^2 T^b}{\partial z^2}\right). \tag{18}$$

The boundary conditions are

$$\text{at } z=b,\quad \psi^b=0,\quad \frac{\partial\psi^b}{\partial z}=0,\quad T^b=0,\ V_\theta^b=r\,\mathrm{Re},$$

$$\text{at } z=-b,\ \psi^b=0,\quad \frac{\partial\psi^b}{\partial z}=0,\quad T^b=0,\quad V_\theta^b=\mathrm{S}\,r\,\mathrm{Re},$$

$$\text{at } r=1,\quad \psi^b=0,\quad \omega^b=\frac{\mathrm{Ma}}{\mathrm{Pr}}f_z\frac{\partial T^b}{\partial z},\quad \frac{\partial V_\theta^b}{\partial r}-\frac{V_\theta^b}{r}=0.$$

The regularity of the velocity and temperature field at the axis imposes $\psi^b=0$, $\omega^b=0$, $V_\theta^b=0$, $\partial T^b/\partial r=0$ at $r=0$.

B. Linear stability analysis

The velocity field is written in the following form:

$$\mathbf{V}(r,\theta,z,t)=\mathbf{V}^b(r,z)+\epsilon\,\mathrm{Real}[(v_r(r,z),\ iv_\theta(r,z),v_z(r,z))\exp(\lambda t+im\theta)], \tag{19}$$

where ϵ is a small parameter, m is the azimuthal wave number and $\lambda=\lambda_r+i\lambda_i$ defines the growth rate λ_r and the frequency λ_i. A similar formulation is used for the pressure p and temperature Θ perturbations. Introducing the expression (19) into the governing equations and boundary conditions (3) through (11) and collecting the leading order terms leads to the governing equations for the perturbation. These equations are written in Appendix A where the exponent b for the base flow has been dropped for legibility. Equations (A1) to (A5) and the associated boundary and regularity conditions lead to a generalized eigenvalue problem. The growth rate λ_r determines the stability of the flow. The neutral curve is found when the leading eigenvalue or complex pair (i.e., the eigenvalue or pair with the largest real part) crosses the imaginary ($\lambda_r=0$) axis.

C. Numerical method and validations

The techniques developed to find the base flow, eigenvalues, eigenvectors, and the neutral curves have been described in a previous study[37] in which many ideas were taken from Chen *et al.*[38] with the following exceptions: a stream function-vorticity formulation is used instead of a primitive variable formulation for the base flow, the mesh is uniformly spaced, the banded matrix system is solved using LAPACK libraries,[39] and the shift-invert transformation to search for eigenvalues is carried out with the help of the ARPACK libraries.[40]

A nonzero azimuthal velocity in the base flow results in complex matrices in the stability analysis, on which LU decompositions must be performed in the ARPACK library. The variables v_r, v_θ, v_z are complex. The phase shift introduced in Eq. (19) for v_θ is useful only if $V_\theta=0$. In that case, the matrices in the eigenvalue problem are purely real and the computational cost can be reduced. The code has been tested with $V_\theta\neq 0$ in the context of isothermal rotating disk flow.[41] Other tests have been performed as detailed in Appendix B.

The key features of the method are summarized here. The set of equations and boundary conditions are discretized by a standard second-order accurate finite-difference scheme. For a given set of parameters, a steady state solution is computed using a Newton-Raphson algorithm. Zero velocity and temperature fields serve as the initial guess. However, for a few cases at larger values of Re, a solution from an intermediate Re value has been used as an initial guess. The neutral curve is found, with all parameters except one (typically Ma) fixed, by computing the base flow and identifying the leading 20 to 40 eigenvalues and then iterating with a secant method to find the zero of λ_r(Ma). The complex shift is carefully chosen along the imaginary axis either to follow the leading eigenvalue or to monitor any new leading eigenvalue that might cross the imaginary axis.

Except when mentioned, all results presented are performed on a $[r\times z]=[51\times 81]$ uniform grid which proved to be a good compromise between accuracy and computational cost (see Appendix B).

III. RESULTS AND DISCUSSION

The base flow generated by Marangoni convection in the full-zone or half-zone configuration is well-known. Section III A explains how the azimuthal velocity affects the Marangoni convection in the full-zone configuration. Section III B discusses the stability of this flow. The case $\mathrm{S}=-1$ is highlighted as this configuration has interesting z-symmetry and is sensitive to an instability that exists even in the absence of Marangoni convection. An energy analysis is carried out in Section III C, providing insight into the physical mechanisms of the instabilities and a general overview of the effect of rotation.

In all cases the Prandtl number is fixed to 0.02, the value most commonly used for molten silicon, and the aspect ratio b is equal to 1. Since the Prandtl number is small and the first bifurcation occurs at a moderate value of the effective viscous Reynolds number (based on the velocity in the bulk flow), the temperature field remains close to the conductive state represented in Fig. 1 (right). For a purely conductive state, the value of the maximum temperature is 1.06 at the free surface for $z=0$. The thermal convection only mildly affects both the temperature gradient along the free surface in the base flow and the instability mechanisms. To confirm the hydrodynamic nature of the instability, a few computations for selected values in the (Re,S) plane have been carried out. These computations were performed by introducing two numerical artifacts. First, f_z is set to 0 in the perturbation boundary conditions (A7). This is artificial but allows for evaluation of the thermocapillary contributions as possible sources of destabilization. Then in a second computation, the base flow velocity (V_r^b and V_z^b) is also set to 0 in the energy equation (18). This corresponds to a physical situation: the limiting case for $\mathrm{Pr}=0$ leading to a purely conductive temperature distribution and thus a prescribed thermocapillary driving force along the free surface. Some quantification of the variation resulting from these thresholds is given in Appendix C.

A. Base flow

The base flow for either $\mathrm{Re}=0$ or $\mathrm{Ma}=0$ is first described, thus considering only one driving source. For

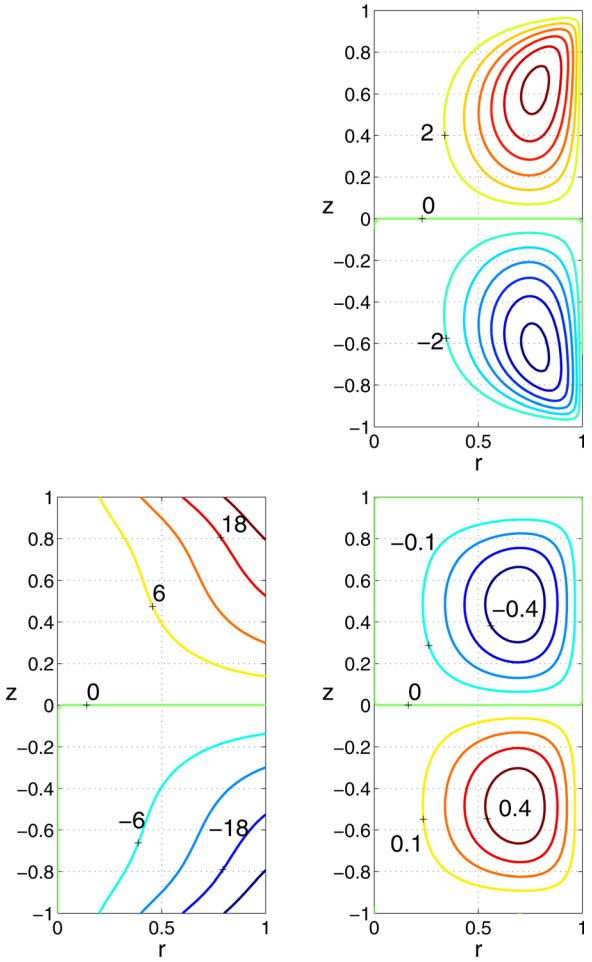

FIG. 2. (Color online) Azimuthal velocity (left) and streamlines (right). Top: Ma = 30, Re = 0. Bottom: Ma = 0, Re = 30, S = −1.

Re = 0, the variation of surface tension with temperature on the free surface drives the flow from the hot spot ($z = 0$) toward the cold spot ($z = \pm b$). Figure 2 (right top) shows the two symmetric recirculations in the meridional plane, counterclockwise in the upper plane and clockwise in the lower. When there is no Marangoni convection, the base flow consists of an azimuthal flow due to the rotation of the disks represented in Fig. 2 (left) and an additional meridional flow in Fig. 2 (right bottom) which is a consequence of the axial variation of the azimuthal flow. One or more recirculating cells form depending on the value of S.

The case S = 0, sometimes called the rotor-stator configuration, has only one recirculating cell if the Reynolds number is not too large. The rotor-stator configuration with a fixed rigid wall at $r = 1$ has been investigated numerically by Daube[42] among other experimental or numerical studies.[43,44] In the exact counter-rotating configuration (S = −1), the meridional recirculating cells, represented in Fig. 2 (right bottom), are opposite to those generated by Marangoni convection. The flow is directed outward along the disks and inward in the symmetry plane.

Now cases with both Marangoni convection and rotation are described. For a given value of Marangoni number, as the rotation rate is increased, two regimes can be observed. For illustration purposes, Ma = 30 is selected because this value is close to the first bifurcation in the case without rotation. In Section III B, perturbations are described at the actual critical Ma values, many of which are below 30.

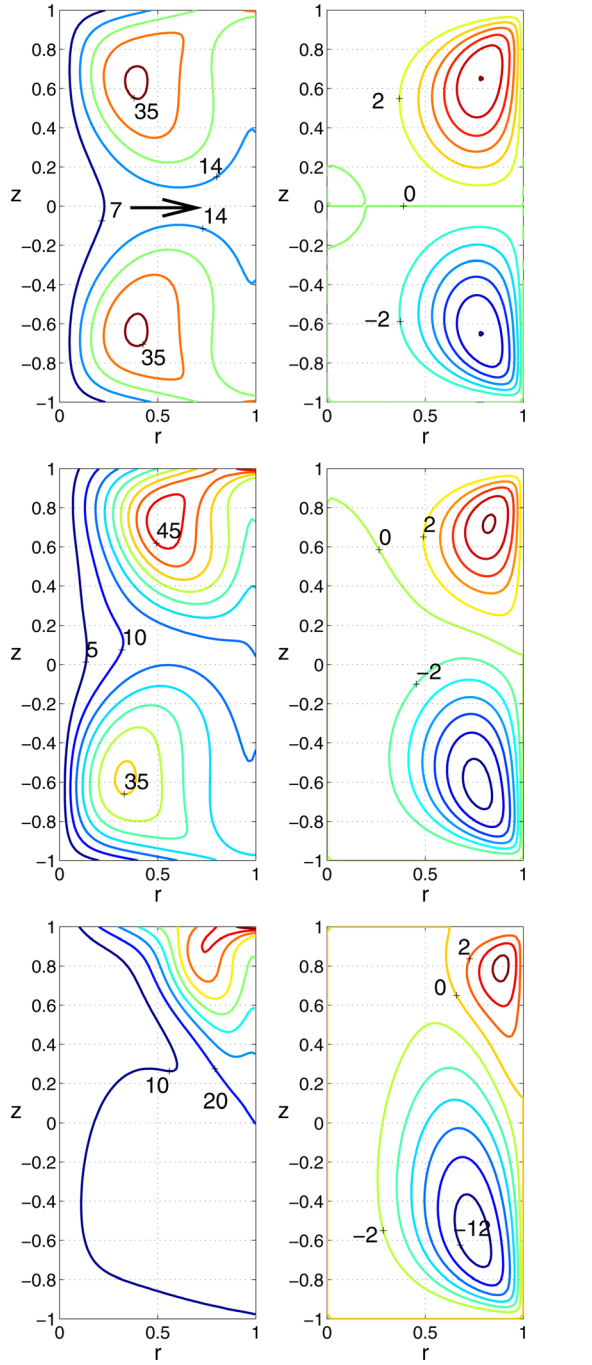

FIG. 3. (Color online) Azimuthal velocity (left) and streamlines (right) for Ma = 30. Top: Re = 30, S = 1. Middle: Re = 50, S = 0.5. Bottom: Re = 100, S = 0.

In the first combined regime, referred to throughout as the weak rotation regime, Marangoni convection dominates the flow and the angular momentum $r\,V_\theta$ is strongly convected. Angular momentum acts almost as a passive scalar. This is illustrated in Fig. 3 (left) where for a fixed z, V_θ^2 is not necessarily increasing with r and large values of V_θ^2 are found in the interior of the domain. In Fig. 3 (left top), the maximum of the azimuthal velocity is not found at $r = 1$ and $z = \pm 1$ as might have been expected but at $r \sim 0.4$ and $z \sim \pm 0.65$. Interestingly, the maximum azimuthal velocity of

the flow is approximately 36 which is larger than the maximum azimuthal velocity of the disk. Even larger values of azimuthal velocity, and therefore angular momentum, could be reached in the flow if not for the dissipative effects of viscosity. The contours for the azimuthal velocity and the stream function in the case $S=-1$ with $Ma=30$ and $Re=30$ (not shown) are almost the same as those presented in Fig. 3 (top) except V_θ is odd with respect to z.

Another observation is that for $Re=30$ (which is considered weak rotation) and $Ma=0$, the meridional flow due to rotation of the disks is much smaller than that induced by purely Marangoni convection with $Ma=30$ and $Re=0$ (see Fig. 2 (right)). The interaction between both sources of motion is not straightforward. Recirculations in the direction opposite to the Marangoni flow (due to counter-rotation $S=-1$) might be expected to cancel out part of the Marangoni flow. Surprisingly, a weak counter-rotation may enhance the Marangoni recirculation. In fact, as Re increases from zero, for any value of S the maximum value of $|\psi|$ initially increases before being damped. The explanation of this phenomenon is understood by the fact that $\partial\left(V_\theta^{b^2}/r\right)/\partial z$ is a source term in Eq. (15). The arrow in Fig. 3 (left top) illustrates the direction in which the flow is driven by this source. The square in this expression indicates that the parity of V_θ with respect to z is not important. Thus for $S=1$ and $S=-1$, the strong Marangoni flow convects and redistributes angular momentum. The axial variation of the angular momentum then either weakly reinforces the Marangoni flow or at least does not oppose this flow.

For $S=0.5$ and $S=0$, there is no longer symmetry with respect to $z=0$. The recirculation close to the upper rotating disk is weakened while the other is enhanced. In the absence of Marangoni convection, a faster upper rotating disk would generate one large clockwise recirculation. When Marangoni convection is added to this rotation, the lower half of the meridional plane is driven in the clockwise direction by both sources. Thus the enhancement of Marangoni convection in Fig. 3 (bottom right) is probably due to superposition of both source terms.

The case of stronger rotation is presented in Fig. 4. Even though the flow does not yet have all the properties of a flow dominated by rotation, this particular value of $Re=100$ is selected because it is of interest for the stability analysis in the next section. The first manifestations of the Taylor-Proudman theorem[45] can be observed: the meridional flow is weakened by rotation, the maximum value of ψ has dropped from roughly 12 to 8. The similarities between $S=-1$ and $S=1$ in Fig. 4 are remarkable. For these co-rotating and counter-rotating limits, the envelopes of contours of V_θ nearest the free surface always have similar shapes (though opposite symmetries). This holds both for small Re when V_θ is convected by the Marangoni flow (as in Fig. 3, top left) and for larger Re where rotation (either co or counter) begins to dominate (as in Fig. 4, left).

Conversely, the behavior of the weaker flow in the region $0<r<0.5$ is different for $S=-1$ and $S=1$. For $S=1$, the azimuthal velocity closely mimics solid body rotation and the inner meridional circulations (probably driven

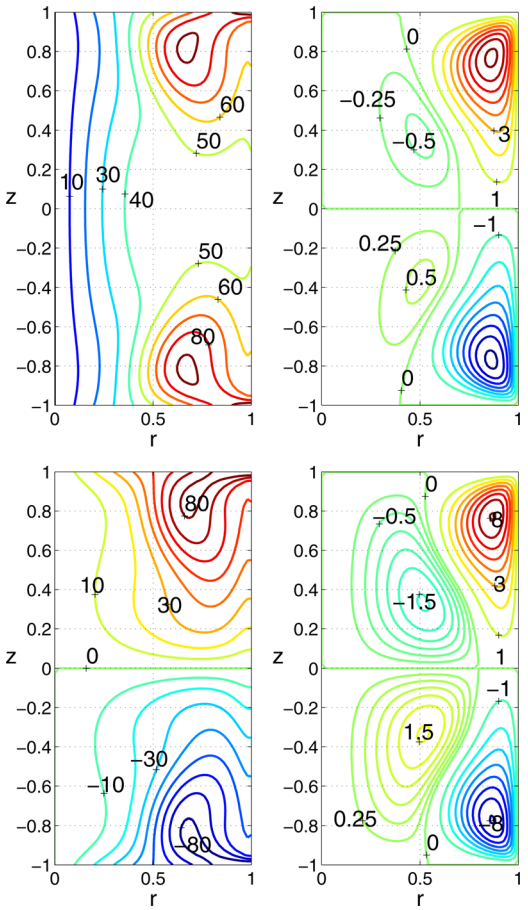

FIG. 4. (Color online) Azimuthal velocity (left) and streamlines (right) for $Ma=30$, $Re=100$. Top: $S=1$. Bottom: $S=-1$. The isovalues are non-equally spaced for the stream function. The step is 1 for recirculations close to the free surface and 0.25 for recirculations close to the axis.

by viscous coupling to the outer circulations) are weaker compared to that for $S=-1$ (as the latter inner circulations are enhanced by differential disk rotation).

For $Re=200$, $Ma=30$ and $S=-1$ (not represented), the maximum value of ψ is close to 4.8 and the flow driven by Marangoni convection is confined near the free surface $r>0.8$. The azimuthal velocity is no longer convected by the weak Marangoni convection. The limit between weak and strong rotation regime is S dependent. For example, $Re=100$ is considered to be in the weak rotation regime for $S=0$ while it is almost in the strong rotation regime for $S=\pm1$. These symmetric (co and counter-rotating) configurations are more efficient for damping the Marangoni convection.

B. Linear stability analysis

The critical values of Ma have been determined in the two dimensional parameter space (Re,S) for $0\le Re\le 150$ and $-1\le S\le 1$ with increments of 1 and 0.05, respectively (see Fig. 5). The azimuthal modes $m=1$ and $m=2$ compete to be critical for almost all cases. Modes $m=0$, 3, 4, 5, 6 have also been checked, and are not critical except in the case near $S=-1$ where $m=3$ is involved. The modes in the bottom right corner of Fig. 5 correspond to $m=2$ bifurcations, though $m=3$ bifurcations are actually critical over some of this small region near $S=-1$, as discussed below.

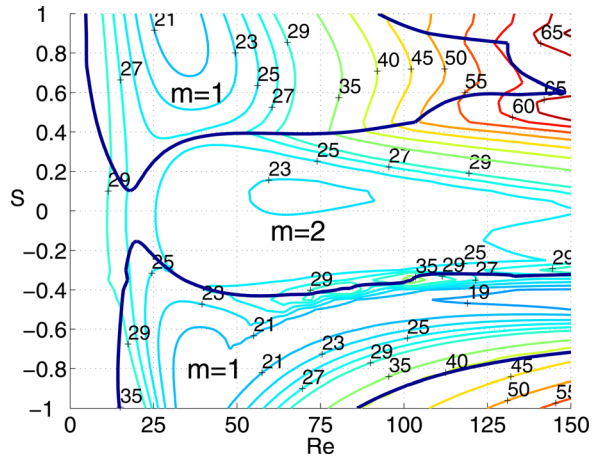

FIG. 5. (Color online) Isovalues of Ma_c for $m=1$ or $m=2$. The thicker lines (dark blue) delimit the regions where $m=1$ or $m=2$ is the critical mode.

The first observation is that for $Re > 50$, it is more effective to set the angular velocity ratio S close or equal to ± 1 to stabilize the flow. As mentioned in Section III A this is due to the fact that for these angular velocity ratios the strong rotation regime is quickly reached. The similarity between the effect of rotation on the Marangoni flow for $S=1$ and $S=-1$, discussed earlier for the base flow, is again quite striking when comparing the evolution of the critical Marangoni number and the switching between $m=1$ and $m=2$. As a second observation, for all values of S, the critical Marangoni number always has a minimum at a value of $Re \neq 0$. This minimum is obtained in the range $25 < Re < 75$, depending on the value of S. Thus, there is always a possible value of rotation that will destabilize the Marangoni flow.

The case $S=1$ illustrates the destabilization of the flow by weak rotation and the competition between the eigenmodes $m=1$ and $m=2$. In Fig. 6, the critical value of Ma is plotted as a function of Re. For $Re=0$, the most unstable mode is stationary, with $m=2$ and $Ma_c=31.1$ based on the coarsest grid used (51×81). The critical Marangoni value for $m=1$ is slightly larger and equal to 35.2 and corresponds to a Hopf bifurcation ($\lambda_i = \pm 19.9$). For $Re > 0$, the transition

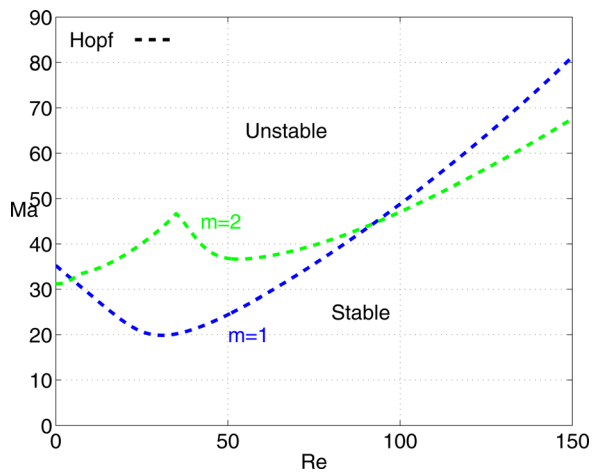

FIG. 6. (Color online) Neutral curves of Ma_c for $m=1$, 2 as function of Re for $S=1$.

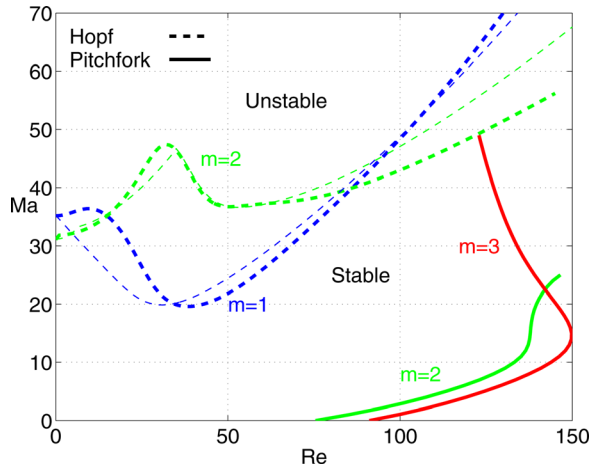

FIG. 7. (Color online) Neutral curves (Re,Ma) for $S=-1$ for $m=1$, 2, 3. Thick solid lines are for transition to stationary flow and thick dashed lines for transition to periodic flow. The thin dashed lines correspond to the neutral curves for $S=1$ from Fig. 6.

is always associated with a transition to a periodic flow. The mode $m=1$ becomes critical for $Re \sim 5$ and the value of Ma_c drops to 19.9 at $Re=30$. For $Re > 67$, the isorotation is sufficiently strong to stabilize the Marangoni flow and $Ma_c > 31.1$. The shape for the neutral curve for $m=1$ is quite smooth while the curve for $m=2$ shows abrupt changes of slope at $Re \sim 6$ and $Re \sim 35$. This is due to the fact that the $m=1$ branch is generated by a unique eigenmode called A_1, while for $m=2$ the curve is generated successively by branches A_2, B_2, and C_2, defined later in the energy analysis (Section III C).

The exact counter-rotating configuration $S=-1$ has some features that need special attention. The neutral curves are represented in Fig. 7. Just as similarities in the base flow between $S=1$ and $S=-1$ were emphasized, there are similarities between the neutral curves starting at $Re=0$. The $S=1$ neutral curves have been superimposed on the $S=-1$ curves in Fig. 7 to demonstrate this similarity.

The dashed $S=-1$ neutral curves are associated with transitions to periodic flow (with the small exception of $m=2$ and $Re < 1$ which cannot be seen due to the axis scale). A new feature for $S=-1$ is a closed stable region delimited by two other neutral curves starting at $Ma=0$, $Re_c \sim 76$ and $Re_c \sim 91$ for $m=2$ and $m=3$, respectively. These two curves are due to the strong counter-rotation of the disks which induces its own instability with a transition to a stationary flow. A small Marangoni convection stabilizes this instability so that above $Re=76$, the neutral curves also define a minimum Marangoni number under which the flow is unstable. Additionally, an upper limit for Reynolds number is found around 142, above which the base flow is unstable for any Marangoni number. In Fig. 5, these instabilities would correspond to a narrow region close to $S=-1$ and are not represented. In fact, this instability is very specific and sensitive to the symmetry. For $Ma=0$, the critical Reynolds number increases sharply with S (for $S=-0.93$ and $m=2$, $Re_c > 250$).

However, there are strong differences between the $S=-1$ eigenvectors and those of other values of S, even

when the neutral curves behave similarly. For any other angular velocity ratio, only one propagating wave is selected at a given Reynolds number. In contrast, each Hopf neutral curve for $S=-1$ corresponds to a pair of propagating waves.

These rotating azimuthal waves should not be confused with those seen at $Re=0$ for a Hopf bifurcation. The latter would correspond to those studied in the half-zone model[46] and discussed in detail in the Rayleigh-Bénard configuration.[47] In both studies the initial standing waves, which result from superposition of the rotating waves traveling in opposite directions, eventually become unstable in favor of one rotating wave in the non-linear regime. With no azimuthal velocity in the base flow ($Re=0$), the matrices in the eigenvalue problem have real coefficients. Thus, for complex-conjugate eigenvalues, the eigenvectors are also complex conjugate. These eigenvalues are repeated and the rotating wave result can be recovered using either $m>0$ or $m<0$. For $Re=0$, each eigenvector also has symmetry (symmetric or antisymmetric) with respect to the mid-plane.

In contrast, for $S=-1$, $Re>0$ two complex conjugate eigenvector pairs exists and computing them requires use of both $m>0$ and $m<0$.

For $m>0$, the eigenvalue with a positive (negative) imaginary part corresponds to a wave propagating with the lower (upper) disk and the corresponding kinetic energy of each eigenmode is distributed accordingly. Thus, it is expected that in a non-linear computation, starting with perturbations of equal amplitude on each eigenmode, will result in two waves traveling in opposite directions, the upper in the direction of the top disk and the lower in the direction of the bottom disk, rather than a standing wave. The stability of this state is beyond the scope of the present study.

C. Energy analysis

One of the goals of this study is to give an overview of the effect of rotation on the Marangoni flow. The mechanisms of the instabilities have already been presented in the non-rotating half-zone configuration, either with an energy analysis[32,48] or analogy to a thin vortex ring.[49] In the vortex ring analogy, the recirculation (or meridional) flow is considered as a vortex ring. The instability mechanism is inviscid and associated with straining the vortex. In the energy analysis, two regions where the base flow provides energy to the perturbation have been observed.[48] These include the region at the periphery of the recirculation where a centrifugal-like mechanism takes place and a region in the core of the vortex (close to the extremum of the stream function) that recovers the strain-induced mechanism proposed in the vortex ring analogy. The term centrifugal should be here considered with caution as it is not associated with azimuthal velocity, but rather with the meridional flow, and could also be considered a shear layer instability.

In the energy analysis, the sources of local production can be decomposed into different contributions. For instance in Ref. 32, seven possible sources of destabilization are listed. Following the spirit of this analysis, the sources of local production are decomposed here. An azimuthal velocity in the base flow adds more potential sources and tracking each contribution in the entire (Re,S) plane proved to be almost intractable. As a strong simplification, the contributions were grouped in two categories: those associated with the meridional base flow (recovering those listed in Ref. 32) and those associated with the azimuthal velocity V_θ (new terms). A third category, the contribution of the Marangoni forces along the free surface, was never significant in the energy balance. This is a common feature for small Prandtl number liquids and an additional argument in favor of the hydrodynamic nature of the instability. Even with just two contributions, no simple dependence was found. One difficulty arises from the fact that $m=1$ and $m=2$ branches alternate as critical. However, even when studied separately, different eigenmodes with fixed wave number can become critical as Re and S vary, and each usually has a different instability mechanism. Finally, even for a given eigenmode and wave number, contributions sometimes vary in a non-monotonic way.

In order to shed some light on the effect of rotation, the eigenvectors are represented by a scalar function, namely the local kinetic energy of the perturbation $\sqrt{v_r^2+v_\theta^2+v_z^2}\, r\, d\theta$, normalized so that the maximum is 1. For a general flow, the local energy production and the local kinetic energy of an eigenmode will not necessarily coincide. For instance, in an open flow configuration it is common that these spatial localizations will differ. However, for this closed geometry, and in the absence of boundary layers, some conclusions based on the spatial localization of the kinetic energy of the eigenmode may be drawn.

In Fig. 8, for $Re=0$ and $Ma=30$, all the eigenmodes that become critical in some region of the (Re,S) plane (see Fig. 9) are represented. The eigenvalues and the associated eigenvectors are labeled with a letter and subscript, the latter of which indicates the critical azimuthal wave number. The eigenvectors can also be distinguished according to their midplane reflection symmetry as in Ref. 17. The eigenvectors represented at the top of Fig. 8 (namely C_2, A_2, and B_1 and its complex conjugate A_1) are antisymmetric such that the perturbations v_r and v_θ are odd and v_z is even with respect to z. Those represented at the bottom (D_2, C_1 and B_2) are symmetric, with perturbations v_r and v_θ even and v_z odd with respect to z, thus maintaining the symmetries of the base flow. Not shown is a mode with wave number 1 which sits between C_2 and D_2 at $Ma=30$, but never becomes critical at any combination of (Re,S) studied.

The symmetry is not revealed by the kinetic energy which is always even with respect to z. The antisymmetric modes, with axial flow through the symmetry plane, are not allowed in the half-zone model, which is more constrained than the full-zone model. Therefore, the eigenmode that is most similar to the critical mode observed in the half-zone model is B_2. Its kinetic energy exhibits a strong similarity with the regions of production of energy represented in Fig. 7(c) in Ref. 48. For $Re=0$, the eigenmodes B_1, C_1, C_2, D_2 depicted in Fig. 8 each have a maximum at the symmetry plane. This likely arises from the combined contribution at the periphery of both vortices as they extend to the symmetry plane.

In Fig. 9, the thick lines (also represented in Fig. 5) separate the regions for which $m=1$ is critical from the $m=2$

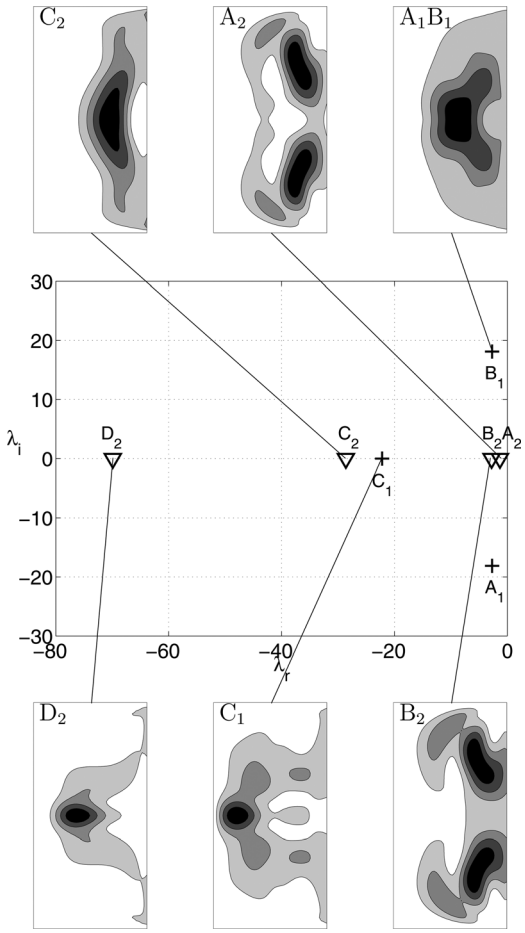

FIG. 8. Leading eigenvalues for Re = 0, Ma = 30, $m = 1$ and $m = 2$, and associated kinetic energy of the leading eigenmodes.

regions, while the thin lines separate the different eigenmodes within each region. For specific (Re,S) combinations, an eigenmode that is representative of the entire region is visualized. A word of caution should be provided at this point. The choice for the letter to label the eigenmode in a region is potentially arbitrary, as eigenvalues may merge at some points in the parameter space. Thus, the label depends on the path chosen to reach the region. The map has been established in the following way. Starting at a given S, m, and Re = 0, the Reynolds number was increased from 0 to 150 while the Marangoni number was maintained at Ma_c. Furthermore, in the narrow region $\mathrm{S} \sim -0.35$, $100 \leq \mathrm{Re} \leq 150$ no label has been given because the modes alternate between A_1, B_1, C_1, and distinguishing the critical mode is likely to be resolution dependent.

When rotation is involved, the symmetry is lost (except for $\mathrm{S} = \pm 1$) and one can observe in Fig. 9 that most of the kinetic energy of the eigenvector is produced either by the upper or the lower vortex. The mechanism suggested for the single vortex in the half-zone configuration could be extended to describe these rotating cases. The symmetry is recovered for S = 1 or Re = 0. This is illustrated by C_2 in Fig. 9 which represents a point close to S = 1 where energy production appears in both the upper and lower regions. As S approaches 1, the energy production in the lower region grows further to match that in the upper region.

To better describe the disturbance flow, the eigenvectors corresponding to velocity and temperature perturbations for two illustrative cases are shown in Fig. 10 and Fig. 11. The top and the bottom contours represent, at a given time, the perturbations in two meridional planes shifted by $\pi/(2m)$. The perturbations are normalized such that $v_z = 1$ at $r = 1$ and $z = 0$. For this small Prandtl number, the temperature perturbation is three orders of magnitude smaller than the perturbation velocities. The corresponding base flows for these cases are qualitatively the same as those presented in Fig. 3 (middle and bottom). The only significant difference is quantitative—the stream function extrema are approximately 20% less, consistent with critical Marangoni numbers that are smaller than Ma = 30.

Fig. 10 shows the eigenvector associated with mode A_1. Consistent with the distribution of perturbation kinetic energy of this mode, shown in Fig. 9, the dominant perturbation flow is localized to the top-half of the meridional plane, and away from $r = 0$. There is no discernible coupling between the perturbation flow on the free surface and the temperature perturbation.

The perturbation flow associated with mode B_2 is given in Fig. 11. Here the perturbed flow is concentrated in the lower-half of the meridional plane, away from both the free surface and $r = 0$. This is again consistent with the perturbation kinetic energy shown in Fig. 9.

In these two cases and throughout most of the domain studied, the eigenvectors retain much of the character of corresponding cases without rotation. The primary impact of the rotation is to shift the eigenvector up or down in the meridional plane. This supports the idea that it is the meridional base flow, driven by Marangoni convection, which drives a hydrodynamic instability. Rotation localizes the perturbation flow and the associated kinetic energy.

In addition to the spatial localization, the frequency that characterizes the instability is of interest for practical applications, as there is a strong correlation between the frequency and the striations observed in the grown crystal.[50] For Re = 0 and Ma = 30, the eigenmodes A_2 (critical), B_2, C_1, C_2, D_2 are stationary so that the angular phase velocity of the eigenmode is zero. The complex-conjugate pair A_1, B_1 is associated with a non-zero frequency and corresponds to two traveling waves propagating with angular phase velocities of 19.9 at Ma = 35.2 in the positive and negative azimuthal directions, respectively.

With rotation, for any $\mathrm{S} \neq -1$, the angular phase velocity of the critical mode is nonzero and the eigenvalues of A_1 and B_1 are not a complex-conjugate pair. The frequency λ_i is reported in Fig. 9 for each eigenmode. It is interesting to interpret these frequencies relative to the base flow. For the eigenmodes $m = 2$, as a rough approximation, the angular phase velocity $-\lambda_i/m$ is on the same order of the mean base-flow angular velocity. The perturbation is therefore convected by the base flow in the azimuthal direction. Note that the region over which this mean should be taken is difficult to define and rather arbitrary. As a first example, consider the mode B_2 represented in Fig. 9 at Re = 100, S = 0. The critical Marangoni number is 23.4 and the azimuthal velocity of the base flow differs only

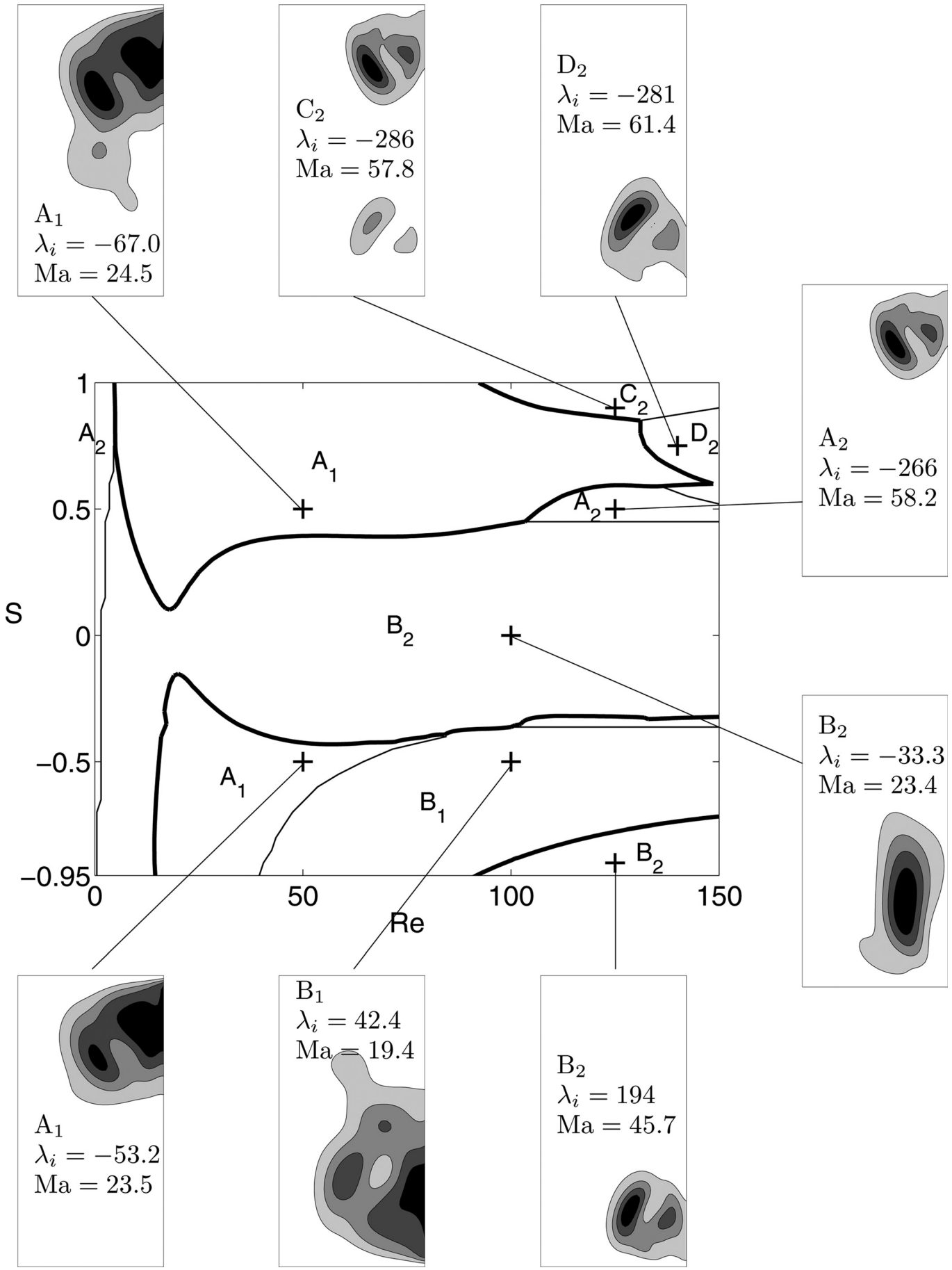

FIG. 9. Distribution of the kinetic energy of the critical eigenmodes for the following (Re,S) values (clockwise from top left to bottom left): A_1 (50, 0.5), C_2 (125, 0.9), D_2 (140, 0.75), A_2 (125, 0.5), B_2 (100, 0), B_2 (125, −0.9), B_1 (100, −0.5), A_1 (50, −0.5).

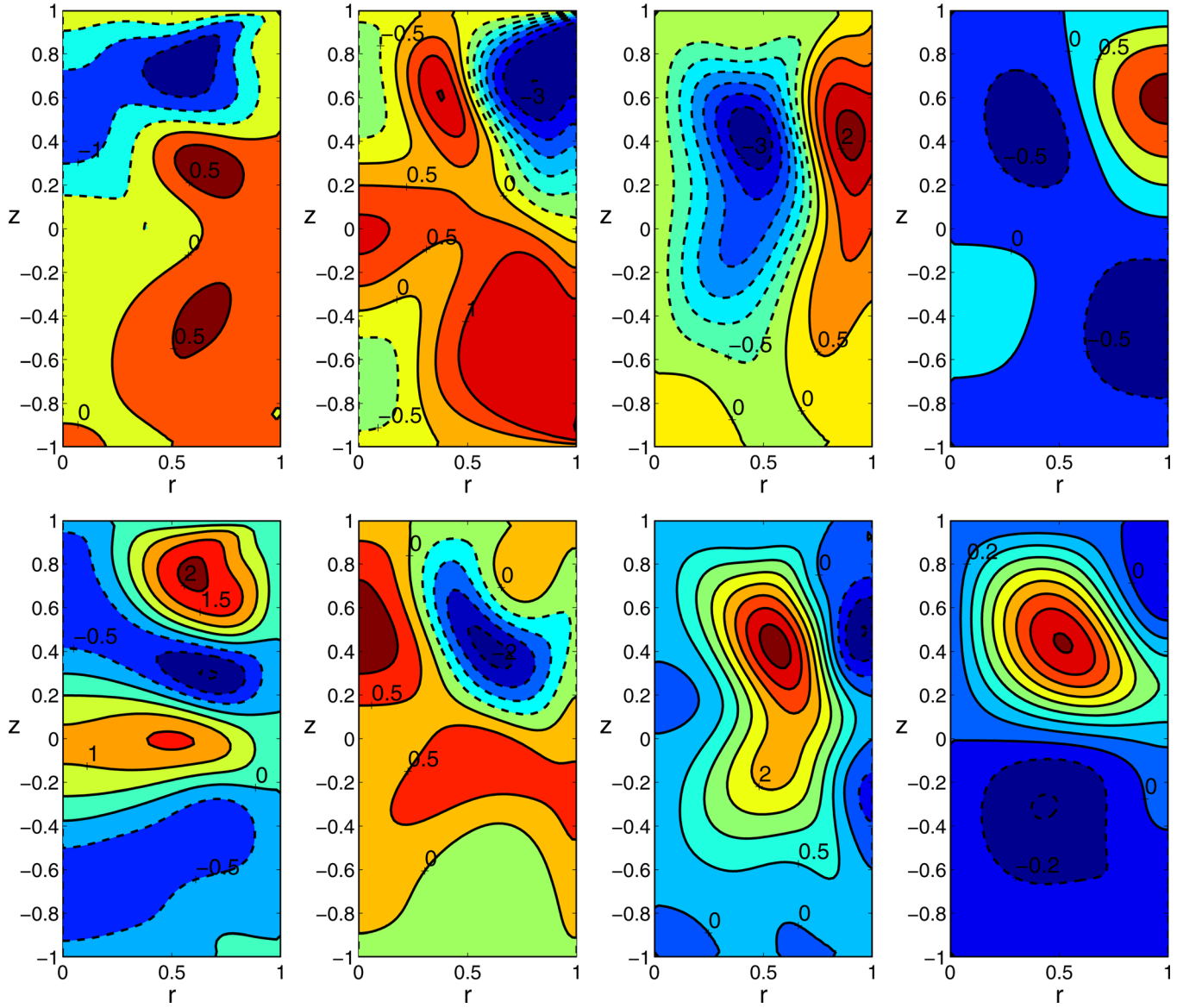

FIG. 10. (Color online) Eigenvectors for $m = 1$, Re = 50, S = 0.5 at Ma = 24.5 corresponding to mode A_1. From left to right radial, azimuthal, axial velocities and temperature. Top: real (v_r, iv_θ, v_z,1000 Θ) and bottom: imaginary (v_r, iv_θ, v_z,1000 Θ).

moderately from the one presented in Fig. 3 (left bottom) for Ma = 30. In the region of the maximum kinetic energy, the mean angular velocity v_θ/r is approximately 16, which is close to $33.3/2$, indicating that the B_2 disturbance is convected with the base flow.

In contrast, for the eigenmodes with $m = 1$, the phase velocity races ahead when compared to the local mean angular velocity of the base flow. Consider, for example, the eigenmode A_1 at Re = 50, S = 0.5. The region over which the mean angular velocity of the base flow should be computed is more difficult to define as there are two local maxima in the distribution of kinetic energy. Depending on the choice of the local maximum, one finds an angular velocity of 55 or 35, which in either case is slower than $67/1$. The same is also verified for A_1 at Re = 50, S = −0.5.

As a last example, the wave associated with the B_1 eigenmode at Re = 100, S = −0.5 has a phase velocity $-42.4/1$ and travels in the negative azimuthal direction. Therefore, this wave also races ahead of the local angular velocity of the base flow which is approximately − 15.

The differences between the phase velocities and the base flow angular velocities for the $m = 1$ eigenmodes can be attributed to the phase velocity of the traveling waves A_1 and B_1. This phase velocity is ±19.9 at Ma = 35.2 for Re = 0. The estimate can be improved by assuming that the phase velocity of the traveling wave relative to the angular velocity of the base flow is only controlled by the intensity of Marangoni convection and is not affected by rotation. The frequency varies monotonically between $\lambda_i = 13.4$ to 25.7 in the range Ma = 20 to 65 for Re = 0.

IV. CONCLUSIONS

The results presented in the full-zone model of the floating-zone technique show that for any angular velocity ratio between the feed rod and the crystal, the effect

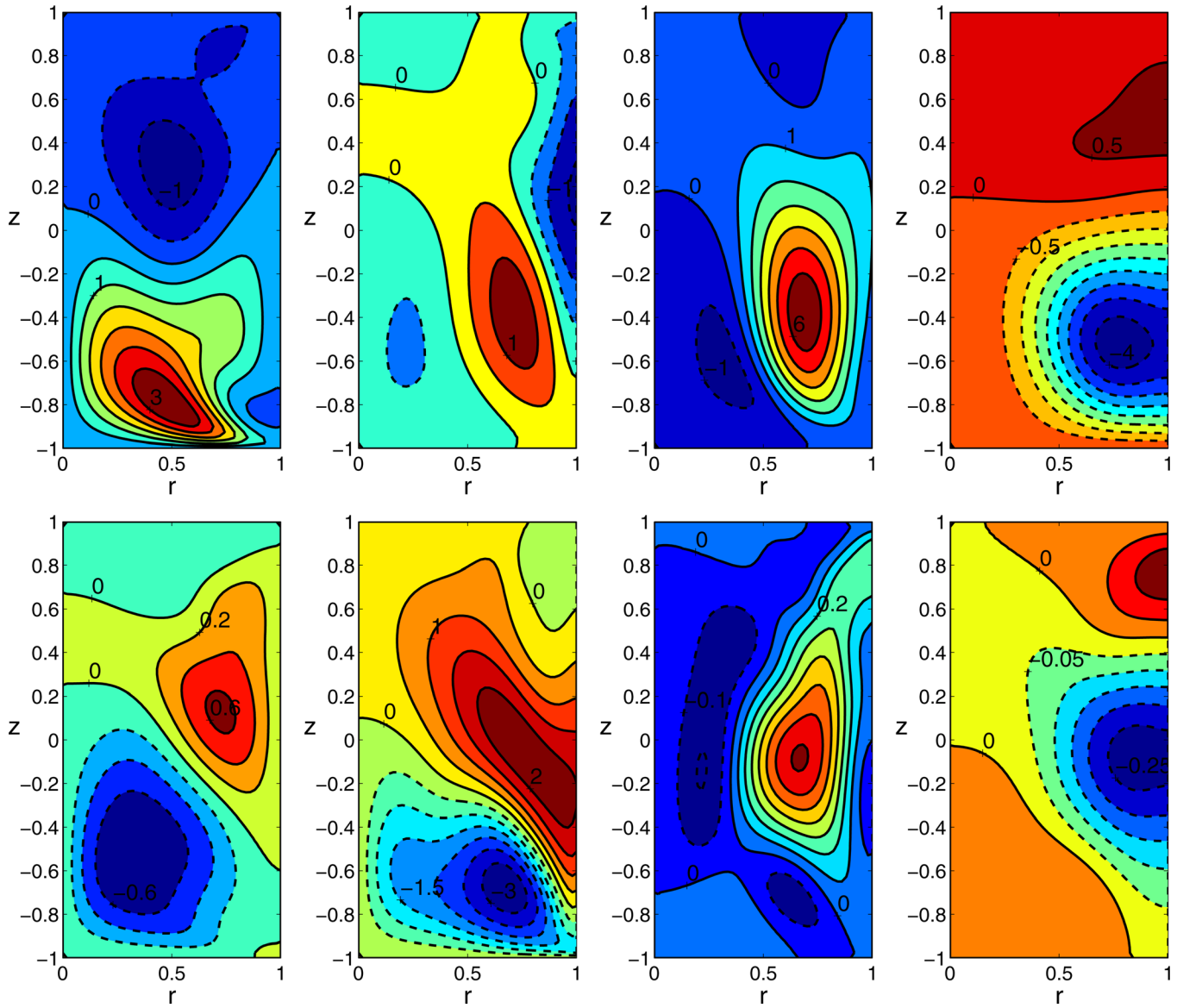

FIG. 11. (Color online) Eigenvectors for $m = 2$, Re = 100, S = 0 at Ma = 23.4 corresponding to mode B_2. From left to right radial, azimuthal, axial velocities and temperature. Top: real (v_r, iv_θ, v_z, 1000 Θ) and bottom: imaginary (v_r, iv_θ, v_z, 1000 Θ).

of rotation on the Marangoni convection is destabilizing in the case of weak rotation but stabilizing for strong rotation. The exception to the latter is the exactly counter-rotating configuration which destabilizes the flow for large rotation rates. The analysis of the role of angular momentum distribution in the base flow provides some understanding about these phenomena.

The systematic linear stability analysis over the Re and S parameter space shows the variety of leading eigenmodes involved in the primary bifurcation. Seven regions in the (Re, S) plane over which leading eigenmodes are critical have been determined. Each eigenmode is characterized by an azimuthal wave number, an angular phase velocity, and the spatial localization of its kinetic energy.

In agreement with previous half-zone studies, the physical mechanism of the instability is mainly attributed to the destabilization of the vortex (or meridional flow) induced by Marangoni convection. This argument is based on the observation that the local kinetic energy of the eigenmode closely follows the vortex localization. The azimuthal velocity enhances or inhibits one of the two vortices generated by Marangoni convection in the full-zone configuration and thus selects if the perturbation will grow in the upper or lower half of the domain. The perturbation is convected by some local mean of the angular velocity of the base flow for cases where m = 2 is critical.

In an experiment or in an industrial crystal-growth process, Re and S can be chosen independently. The instability is quite sensitive to this choice. For two contiguous regions in the (Re,S) plane, the eigenmode can change its azimuthal wave number from $m = 1$ to $m = 2$, change its spatial localization from the lower disk to the upper disk, and change the direction of propagation of the perturbation (in the positive or negative azimuthal direction). Providing practical advice for crystal growers is therefore not an easy task. The first advice would be to choose S either close to 1 or -1 as stabilization is achieved at moderate rotation rates near these extremes. However, values very close to S = -1 coupled

with large Re should be avoided as such flows are prone to an intrinsic isothermal counter rotating disks instability. A second suggestion is to choose a region in the map where the instability is close to the feed rod rather than the crystal so as to achieve a crystal with less impact from striations. Setting the feed rod to the lowest angular velocity and $S \sim -0.8$ may fulfill all these requirements.

This advice should nevertheless be taken with caution as nonlinear combinations of modes and secondary bifurcations have not been addressed in this study and can significantly modify the flow behavior. For instance, with no rotation and small Prandtl number, the half-zone and the full-zone behave quite similarly in the linear stability analysis.[17] However, the three-dimensional, non-linear time integrations presented in Ref. 16 for the full-zone configuration and in Ref. 46 for the half-zone configuration show different behavior. Extending the three-dimensional computations to the entire (Re,S) plane seems out of reach. An alternative is a weakly nonlinear analysis using reduced models.[51] Such models reduce the number of degrees of freedom to a small set that captures the dynamics of the flow. This is achieved by a Galerkin projection of the Navier–Stokes equations on the leading eigenvectors computed by a linear stability analysis. Reduced models are still in the early stages of development and have been primarily tested in simple configurations. They are nevertheless promising. Applying these techniques to the full-zone configuration with rotation is a good challenge and may be helpful for future analysis.

It should also be noted that it is difficult to extrapolate the results presented here to a full-scale crystal growth experiment. For example, in the radiatively heated monoellipsoidal furnace growth and the RF heated growth of Dold *et al.*, convective temperature fluctuations on the free surface of the silicon liquid bridge were approximately 1 K and 5 K, respectively.[1,52] However, temperature gradients at the growth front measured approximately 100 K/cm in the radiatively heated case and 275 K/cm in the RF heated experiment. Thus the effective Marangoni number is highly nonuniform across the free surface in crystal growth. These experiments result in Ma ranging from about 80–90 (for the 1 K fluctuation) up to 10 000 or higher for the steepest gradient at the solidification front. The lower limit is on the same order as the simulations presented here, but the upper limit is well beyond, with strong local thermocapillary flow and significant buoyancy effects. While the work presented here aids in the fundamental understanding of instabilities in liquid bridges, it cannot be directly extended to full-scale crystal growth systems where large gradients at the growth front are maintained to avoid the morphological instability.

However, there is at least one experiment to which this study sheds insight. The $\mathrm{Re}=0$, $m=2$ steady mode is best compared to a half-zone experiment in which a similar perturbation was observed. In Fig. 6 of Takagi *et al.*,[53] the surface flow visualization at $\Delta T = 7K$, just before onset of the periodic flow, shows what appears to be an $m=2$ steady mode. These experiments used molten tin with properties $\mathrm{Pr}=0.01$, $\frac{d\gamma^*}{dT^*} = -0.9\times10^{-4}\,\mathrm{N/mK}$, $\mu = 1.4\times10^{-3}$ Pa-s, where μ is the dynamic viscosity, $\kappa = 2.0\times10^{-5}\,\mathrm{m^2/s}$, and $R^* = 1.5$ mm. At $\Delta T = 7K$, this corresponds to $\mathrm{Ma}=33.8$. While the full-zone tends to have a lower Ma_c as compared to the half-zone, the values are of the same order of magnitude. Thus, the linear stability prediction of $\mathrm{Ma}_c = 31.1$ is very realistic for the onset of the first stationary instability expected in an experiment at $\mathrm{Pr}=0.02$.

ACKNOWLEDGMENTS

Special thanks are due to Professor John S. Walker for suggesting this investigation and sharing with us his great insights into perturbation analyses. We also thank Ivan Delbende, Daniel Henry, Caroline Nore, and Laurette S. Tuckerman for helpful discussions.

APPENDIX A: LINEAR EQUATIONS FOR THE PERTURBATION

The equations for the perturbation are

$$\frac{1}{r}\frac{\partial(rv_r)}{\partial r} - \frac{mv_\theta}{r} + \frac{\partial v_z}{\partial z} = 0, \tag{A1}$$

$$\begin{aligned}&\frac{2}{r}\frac{\partial}{\partial r}(rv_rV_r) - \frac{mv_\theta V_r}{r} + i\frac{mv_rV_\theta}{r} - i\frac{2v_\theta V_\theta}{r}\\ &\quad + \frac{\partial}{\partial z}(v_rV_z) + \frac{\partial}{\partial z}(v_zV_r) + \frac{\partial p}{\partial r}\\ &\quad - \left(\frac{\partial^2 v_r}{\partial r^2} + \frac{1}{r}\frac{\partial v_r}{\partial r} - \frac{(1+m^2)v_r}{r^2} + \frac{2mv_\theta}{r^2} + \frac{\partial^2 v_r}{\partial z^2}\right) = -\lambda v_r,\end{aligned} \tag{A2}$$

$$\begin{aligned}&\frac{1}{r}\frac{\partial}{\partial r}(rv_\theta V_r) + \frac{v_\theta V_r}{r} + i\frac{2mv_\theta V_\theta}{r}\\ &\quad - \frac{i}{r}\frac{\partial}{\partial r}(rv_rV_\theta) - i\frac{v_rV_\theta}{r} - i\frac{\partial}{\partial z}(v_zV_\theta)\\ &\quad + \frac{\partial}{\partial z}(v_\theta V_z) + \frac{mp}{r}\\ &\quad - \left(\frac{\partial^2 v_\theta}{\partial r^2} + \frac{1}{r}\frac{\partial v_\theta}{\partial r} - \frac{(1+m^2)v_\theta}{r^2} + \frac{2mv_r}{r^2} + \frac{\partial^2 v_\theta}{\partial z^2}\right) = -\lambda v_\theta,\end{aligned} \tag{A3}$$

$$\begin{aligned}&\frac{1}{r}\frac{\partial}{\partial r}(rv_rV_z) + \frac{1}{r}\frac{\partial}{\partial r}(rV_rv_z) + i\frac{mv_zV_\theta}{r}\\ &\quad - \frac{mv_\theta V_z}{r} + 2\frac{\partial}{\partial z}(v_zV_z) + \frac{\partial p}{\partial z}\\ &\quad - \left(\frac{\partial^2 v_z}{\partial r^2} + \frac{1}{r}\frac{\partial v_z}{\partial r} - \frac{m^2 v_z}{r^2}\frac{\partial^2 v_z}{\partial z^2}\right) = -\lambda v_z\end{aligned} \tag{A4}$$

$$\begin{aligned}&V_r\frac{\partial\Theta}{\partial r} + v_r\frac{\partial T}{\partial r} + i\frac{m\Theta V_\theta}{r} + V_z\frac{\partial\Theta}{\partial z} + v_z\frac{\partial T}{\partial z}\\ &\quad - \frac{1}{\mathrm{Pr}}\left(\frac{\partial^2\Theta}{\partial r^2} + \frac{1}{r}\frac{\partial\Theta}{\partial r} - \frac{m^2\Theta}{r^2} + \frac{\partial^2\Theta}{\partial z^2}\right) = -\lambda\Theta.\end{aligned} \tag{A5}$$

The boundary conditions are
at $z = \pm b$

$$v_r = 0, \quad v_\theta = 0, \quad v_z = 0, \quad \Theta = 0 \tag{A6}$$

and at $r = 1$

$$\begin{aligned}&v_r = 0, \quad \frac{\partial}{\partial r}\left(\frac{v_\theta}{r}\right) = -\frac{\mathrm{Ma}}{\mathrm{Pr}}f_z\frac{m}{r^2}\Theta,\\ &\frac{\partial v_z}{\partial r} = -\frac{\mathrm{Ma}}{\mathrm{Pr}}f_z\frac{\partial\Theta}{\partial z}, \quad \frac{\partial\Theta}{\partial r} = 0.\end{aligned} \tag{A7}$$

The regularity at the axis imposes
for $m=0$,

$$v_r = 0, \quad v_\theta = 0, \quad \frac{\partial v_z}{\partial r} = 0, \quad \frac{\partial \Theta}{\partial r} = 0, \tag{A8}$$

for $m=1$,

$$\frac{\partial v_r}{\partial r} = 0, \quad \frac{\partial v_\theta}{\partial r} = 0, \quad v_z = 0, \quad \Theta = 0, \tag{A9}$$

and for $m>1$,

$$v_r = 0, \quad v_\theta = 0, \quad v_z = 0, \quad \Theta = 0. \tag{A10}$$

APPENDIX B: BENCHMARKING AND GRID REFINEMENT STUDY

1. Base flow benchmarks

We compare the base flow for the isothermal case (Ma = 0) with an early study by Kobayashi and Wilcox.[23] Values for the minimum of the stream function are given in the caption of their figure 2. Unfortunately, the grid size is not specified. Table I shows that our results are in close agreement with those found by Kobayashi *et al.*[23] especially given that the location of the minimum values are found on grid points which do not necessary align between the two studies. The values given have been converted to match our scaling.

Table II compares our results to Figs. 2 and 6 of a second article by Kobayashi[6] that considered the nonisothermal situation with or without rotation. The heat flux boundary condition at $r=1$ is given by

$$\frac{\partial T^b}{\partial r} = 1 - \frac{\mathrm{Bi}}{Q}(1+QT^b)^4,$$

with $Q=0.0575$ and $\mathrm{Bi}=0.01$. The agreement is good with the exception of three cases. Two cases can be explained as we believe there is an inversion in the caption between Fig. 6 (b) (S = 0) and figure 6 (c) (S = −1) in the article of Kobayashi. For the third case, the large value of Marangoni (Ma = 57.5) requires a fine grid to obtain accurate results.

2. Stability analysis benchmarks

We also benchmarked our code in the half-zone configuration ($b=0.5$) that has been widely studied. The heat flux is zero at the free surface and the temperature at $z=-b$ is set to 1. For Pr = 0.02, the most unstable mode is stationary

TABLE I. Minimum values of the stream function ψ^b for Re = 100, $b=1$ and various S for the isothermal case Ma = 0.

S	51 × 81	101 × 161	Kobayashi[23]
0.5	−0.820	−0.811	−.80
0.0	−1.71	−1.70	−1.70
−0.5	−2.14	−2.12	−2.13
−0.75	−2.12	−2.10	−2.11
−1.	−2.05	−2.03	−2.03

TABLE II. Comparison of the minimum values of the stream function ψ^b for $b=1$, Pr = 0.01.

Ma	S	Re	51 × 81	101 × 161	Kobayashi[6]
0.575	–	0	−0.616	−0.615	−0.618
5.75	–	0	−4.98	−4.98	−4.92
57.5	–	0	−29.5	−30.0	−25.5
5.75	1	100	−2.27	−2.26	−2.27
5.75	0	100	−5.30	−5.30	−1.87
5.75	−1	100	−1.97	−1.96	−5.20

($\lambda_i=0$) with $m=2$. Chen *et al.*[38] found a critical Marangoni Ma = 41.08, Wanschura *et al.*[32] found Ma = 41.24 and Ma *et al.*[27] found Ma = 41.18. We found Ma = 40.91 and Ma = 41.07 on a 41 × 41 and a 81 × 81 grid, respectively. For Pr = 0.01, Shevtsova[54] proposed a benchmark and further computations have been carried out by Gelfgat.[55] The most unstable mode is again steady with $m=2$. We found critical Marangoni values of Ma = 18.924, Ma = 18.952, and Ma = 18.970 on 51 × 51, 81 × 81, and 141 × 141 grids, respectively. In order to check an oscillatory bifurcation, we also computed the $m=5$ mode, which is not the critical mode. On the same grids, Ma = 93.823, 94.047, 94.402, and $\lambda_i\,\mathrm{Pr}/\mathrm{Ma} = 0.0618, 0.0632, 0.0637$ were found. All of these results are consistent with the values given in Table III of Ref. 55, namely Ma = 18.980 for $m=2$ and Ma = 94.702 with $\lambda_i\,\mathrm{Pr}/\mathrm{Ma} = 0.0639$ for $m=5$.

3. Grid dependence study

Table III presents, for select points in the (Re, S) plane, the critical values of Ma, m, and λ_i computed for different grids. The first line (Ma_c values for Re = 0) can be compared to the value found by Houchens and Walker[17] of Ma = 30.92 in their Table A2 and the refined value of Ma = 30.93 in Huang and Houchens.[35] Matching the regularization parameter to their computations ($\alpha=400$) improves the last digit as we find Ma = 30.94 on the 151 × 241 grid. The critical values found for Re = 30, S = 1 match those found by Ma *et al.*[27] as they found a mode $m=1$ and Ma = 995 *.02 = 19.9.

The grid dependence study shows that the critical values vary within 3% from the coarse grid to the refined grid. Thus, a 51 × 81 grid with $\alpha=200$ for the exhaustive study in the (Re, S) plane was used.

4. Computational cost

If a reasonable guess is provided, the secant method converges within 4 to 6 iterations to find a critical value for one (Re, S) combination. The computational cost of one secant iteration depends heavily on the efficiency of solving the linear systems arising from the base flow and eigenvalue problems. A small fraction of time is spent to build the matrix. A direct rather than an iterative method to solve the linear systems proved to be more efficient, especially for the computation of the leading eigenvalues. Each Newton iteration requires one (costly) LU factorization and one back solve (forward elimination and back substitution). Depending on the initial guess, 2 to 10 Newton iterations are needed

TABLE III. Critical values (Ma, m, λ_i) for various grids and select values of Re and S with $\alpha = 200$.

Re	S	51×81	101×161	151×241
0	–	(31.09, 2, 0)	(30.98, 2, 0)	(30.96, 2, 0)
50	−1	(21.81, 1, ±52.07)	(21.77, 1, ±52.12)	(21.76, 1, ±52.12)
50	0	(23.11, 2, − 13.70)	(23.08, 2, − 13.77)	(22.99, 2, − 13.79)
100	0	(23.35, 2, − 33.33)	(23.26, 2, − 33.45)	(23.24, 2, − 33.47)
150	0	(24.81, 2, − 59.26)	(24.71, 2, − 59.23)	(24.69, 2, − 59.23)
30	1	(19.87, 1, − 53.96)	(19.89, 1, − 54.15)	(19.90, 1, − 54.18)
50	1	(24.41, 1, − 76.61)	(24.48, 1, − 76.89)	(24.48, 1, − 76.93)
100	1	(46.96, 2, − 237.8)	(47.50, 2, − 239.4)	(47.59, 2, − 239.4)
150	1	(67.33, 2, − 354.7)	(68.89, 2, − 357.7)	(69.13, 2, − 358.0)

to reduce the norm of the residual below 10^{-10}. The size of the matrix for the base flow is smaller than that for the eigenvalue solver (four variables and real coefficients versus five variables and complex coefficients) thus even if the eigenvalue solver requires only one factorization of the matrix but 100 to 500 back solves, it consumes most of the CPU time and memory. The required number of converged eigenvalues and the distribution of the spectrum, which is problem dependent, may significantly vary the number of back solves and consequently impact the CPU time consumption.

In order to give an estimate of the CPU time and memory usage for one iteration of the secant method for the grids used in Table III, we have set the following arbitrary values $\mathrm{Re} = 140$, $\mathrm{S} = -0.8$, $m = 2$, and $\mathrm{Ma} = 40$. Starting with zero temperature and velocity fields as initial guesses for the base flow, the converged solution is obtained with 9 Newton iterations and 170 back solves to accurately find 40 eigenvalues. For the grids (51×81, 101×161, 151×241), consumption of CPU times are, respectively, 0'16s, 2'20s, and 9'15s. Peak memory usages are 0.3, 2.0, and 6.5 GB. These timings are for a PC computer with 24 GB memory and an Intel i7 $980 \times$ processor (using only one core and the Intel MKL optimized Lapack library). Additional computations were performed using all 6 cores and a direct sparse solver (Pardiso implemented in the Intel MKL library) to illustrate the importance of the optimization of the linear solver. For the finest (151×241) grid, CPU time drops from 9'15s to 1'04s. Another advantage of the direct sparse solver is a lower memory usage (1.3GB for this grid).

TABLE IV. Critical Marangoni numbers and frequencies for selected (Re,S) combination. Three values are presented: (1) for $\mathrm{Pr} = 0.02$, (2) setting f_z to 0 in Eqs. (A7), (3) setting f_z to 0 in Eqs. (A7) and V_r^b and V_z^b to 0 in Eq. (18).

Mode	Re	S	Ma	λ_i
A_1	50	0.5	24.5, 23.6, 21.2	−67.0, −66.4, −66.0
C_2	125	0.9	57.8, 53.9, 48.5	−286, −283, −280
D_2	140	0.75	61.4, 55.2, 49.0	−281, −275, −273
A_2	125	0.5	58.2, 53.8, 48.2	−266, −264, −262
B_2	100	0	23.4, 20.6, 18.5	−33.3, −33.4, −34.4
B_2	125	−0.9	45.7, 43.0, 39.8	194, 193, 191
B_1	100	−0.5	19.4, 18.4, 17.1	42.4, 41.9, 41.3
A_1	50	−0.5	23.5, 22.7, 21.1	−53.2, −52.7, −52.3

APPENDIX C: LIMITING CASE FOR Pr = 0

This appendix only focus on the eight (Re, S) combinations in Fig. 9 which are likely representative of the entire plane. The critical Maranagoni values and the frequency were computed neglecting Marangoni forces in the perturbed flow and for the limiting case $\mathrm{Pr} = 0$. These values are compared to the values for $\mathrm{Pr} = 0.02$ in Table IV. The critical Marangoni number is modified in the worse case by 25% but the frequency is only moderately affected (less than 4% variation). The fact that the critical Marangoni number is lower for $\mathrm{Pr} = 0$ than for $\mathrm{Pr} = 0.02$, suggests that Marangoni forces in the perturbed flow and thermal convection in the base flow are stabilizing. In all cases, the qualitative distribution of the kinetic energy of the leading mode was not significantly changed. The temperature distribution for the base flow was also monitored. The isotherms are qualitatively similar to those presented in Fig. 1 (right). More quantitatively, out of the eight combinations, the maximum deviation from the purely conductive temperature distribution is equal to 0.07 and is found on the free surface for $\mathrm{Re} = 125$ and $\mathrm{S} = 0.5$.

If the temperature distribution in the base flow and the temperature disturbances are not essential for the destabilizing mechanism, they are however crucial in the crystal growth process as temperature oscillations are directly related to crystal defects. As a first approximation, temperature can be considered as a passive scalar.

[1]P. Dold, "Analysis of microsegregation in RF-heated float zone growth of silicon – comparison to the radiation-heated process," J. Cryst. Growth **261**, 1 (2004).
[2]W. Keller and A. Mühlbauer, *Floating-Zone Silicon* (M. Dekker, New York, 1981).
[3]W. Keller, "Experimental influence of some growth parameters upon the shape of the melt interfaces and the radial phosphorus distribution during float-zone growth of silicon single crystals," J. Cryst. Growth **36**, 215 (1976).
[4]G. Ratnieks, A. Muiznieks, L. Buligins, G. Raming, A. Mühlbauer, A. Lüdge, and H. Riemann, "Influence of the three dimensionality of the HF electromagnetic field on resistivity variations in Si single crystals during FZ growth," J. Cryst. Growth **216**, 204 (2000).
[5]T. A. Campbell, M. Schweizer, P. Dold, A. Cröll, and K. W. Benz, "Float-zone growth of $Ge_{1-x}Si_x$($x \leq 10$ at%) single crystals," J. Cryst. Growth **226**, 231 (2001).
[6]N. Kobayashi, "Computer simulation of the steady flow in a cylindrical floating zone under low gravity," J. Cryst. Growth **66**, 63 (1984).
[7]E. Chénier, C. Delcarte, and G. Labrosse, "Stability of the axisymmetric buoyant-capillary flows in a laterally heated liquid bridge," Phys. Fluids **11**, 527 (1999).
[8]T. Kaiser and K. W. Benz, "Floating-zone growth of Silicon in magnetic fields III. Numerical simulation," J. Cryst. Growth **183**, 564 (1998).
[9]R. Bennacer, A. A. Mohamad, and E. Leonardi, "The effect of heat flux distribution on thermocapillary convection in a side-heated liquid bridge," Numer. Heat Transfer Part A **41**, 657 (2002).
[10]A. Y. Gelfgat, A. Rubinov, P. Bar-Yoseph, and A. Solan, "On the three-dimensional instability of thermocapillary convection in arbitrarily heated floating zones in microgravity environment," Fluid Dyn. Mater. Process. **1**, 21 (2005).
[11]F. Preisser, D. Schwabe, and A. Scharmann, "Steady and oscillatory thermocapillary convection in liquid columns with free cylindrical surface," J. Fluid Mech. **126**, 545–567 (1983).
[12]I. Ueno, S. Tanaka, and H. Kawamura, "Oscillatory and chaotic thermocapillary convection in a half–zone liquid bridge," Phys. Fluids **15**, 408 (2003).
[13]H. Kawamura, K. Nishino, S. Matsumoto, and I. Ueno, "Space experiment of Marangoni convection on International Space Station," in *14th*

International Heat Transfer Conference (ASME, Washington, DC, USA, 2010), Vol. 8, pp. 343–362.
[14]H. C. Kuhlmann, *Thermocapillary Convection in Models of Crystal Growth*, Springer tracts in modern physics (Springer, Berlin, 1999), Vol. 152.
[15]M. Lappa, "Three-dimensional numerical simulation of Marangoni flow instabilities in floating zones laterally heated by an equatorial ring," Phys. Fluids **15**, 776 (2003).
[16]O. Bouizi, C. Delcarte, and G. Kasperski, "Stability study of the floating zone with respect to the Prandtl number value," Phys. Fluids **19**, 114102 (2007).
[17]B. C. Houchens and J. S. Walker, "Modeling the floating zone: Instabilities in the half zone and full zone," J. Thermophys. Heat Transfer **19**, 186 (2005).
[18]J. R. Carruthers and M. Grasso, "Studies of floating liquid zones in simulated zero gravity," J. Appl. Phys. **43**, 436 (1972).
[19]C. H. Chun, "Marangoni convection in a floating zone under reduced gravity," J. Cryst. Growth **48**, 600 (1980).
[20]C. H. Chun and W. Wuest, "Suppression of temperature oscillations of thermal Marangoni convection in a floating zone by superimposing of rotating flows," Acta Astronaut. **9**, 225 (1982).
[21]Y. Kamotani and J. Kim, "Effect of zone rotation on oscillatory thermocapillary flow in simulated floating zones," J. Cryst. Growth **87**, 62 (1988).
[22]C. E. Chang and W. R. Wilcox, "Inhomogeneities due to thermocapillary flow in floating zone melting," J. Cryst. Growth **28**, 8 (1975).
[23]N. Kobayashi and W. R. Wilcox, "Computational studies of convection due to rotation in a cylindrical floating zone," J. Cryst. Growth **59**, 616 (1982).
[24]C. E. Chang, "Computer simulation of convection in floating zone melting I. Pure rotation driven flows," J. Cryst. Growth **44**, 168 (1978).
[25]G. M. Harriott and R. A. Brown, "Flow in a differentially rotated cylindrical drop at moderate Reynolds number," J. Fluid Mech. **144**, 403 (1984).
[26]J. S. Walker, L. Martin Witkowski, and B. C. Houchens, "Effects of a rotating magnetic field on the thermocapillary instability in the floating zone process," J. Cryst. Growth **252**, 413 (2003).
[27]N. Ma, J. S. Walker, and L. Martin Witkowski, "Combined effects of rotating magnetic field and rotating system on the thermocapillary instability in the floating zone crystal growth process," J. Heat Transfer **126**, 230 (2004).
[28]B. C. Sim and A. Zebib, "Effect of free surface heat loss and rotation on transition to oscillatory thermocapillary convection," Phys. Fluids **14**, 225 (2002).
[29]A. Y. Gelfgat, A. Rubinov, P. Z. Bar-Yoseph, and A. Solan, "Numerical study of three-dimensional instabilities in a hydrodynamic model of Czochralski growth," J. Cryst. Growth **275**, e7 (2005).
[30]W. Shi, Y. Li, M. K. Ermakov, and N. Imaishi, "Stability of thermocapillary convection in rotating shallow annular pool of silicon melt," Microgravity Sci. Technol. **22**, 315 (2010).
[31]H. Minakuchi, Y. Okano, and S. Dost, "A three-dimensional numerical study of Marangoni convection in a floating full zone," Int. J. Mater. Prod. Technol. **22**, 151 (2005).
[32]M. Wanschura, V. M. Shevtsova, H. C. Kuhlmann, and H. J. Rath, "Convective instability mechanisms in thermocapillary liquid bridges," Phys. Fluids **7**, 912 (1995).
[33]G. Kasperski and G. Labrosse, "On the numerical treatment of viscous singularities in wall-confined thermocapillary convection," Phys. Fluids **12**, 2695 (2000).
[34]E. Chénier, C. Delcarte, G. Kasperski, and G. Labrosse, "Sensitivity of the liquid bridge hydrodynamics to local capillary contributions," Phys. Fluids **14**, 3109 (2002).
[35]Y. Huang and B. C. Houchens, "Numerical linear stability analysis of a thermocapillary driven liquid bridge with magnetic stabilization," J. Mech. Mater. Struct. (to be published).
[36]L. Martin Witkowski and J. S. Walker, "Flow driven by Marangoni convection and rotating magnetic field in a floating-zone configuration," Magnetohydrodynamics **37**, 112 (2001).
[37]L. Martin Witkowski and J. S. Walker, "Solutocapillary instabilities in liquid bridges," Phys. Fluids **14**, 2647 (2002).
[38]G. Chen, A. Lizée, and B. Roux, "Bifurcation analysis of the thermocapillary convection in cylindrical liquid bridges," J. Cryst. Growth **180**, 638 (1997).
[39]E. Anderson, Z. Bai, C. Bischof, S. Blackford, J. Demmel, J. Dongarra, J. D. Croz, A. Greenbaum, S. Hammarling, A. McKenney, and D. Sorensen, *LAPACK Users' Guide*, 3rd ed. (SIAM, Philadelphia, PA, 1999).
[40]R. B. Lehoucq, D. C. Sorensen, and C. Yang, *ARPACK Users' Guide: Solution of Large-Scale Eigenvalue Problems with Implicitly Restarted Arnoldi Methods* (SIAM, Philadelphia, PA, 1998).
[41]C. Nore, L. M. Witkowski, E. Foucault, J. Pécheux, O. Daube, and P. L. Quéré, "Competition between axisymmetric and three-dimensional patterns between exactly counter-rotating disks," Phys. Fluids **18**, 054102 (2006).
[42]O. Daube, "Numerical simulation of axisymmetric vortex breakdown in a closed cylinder," in *Vortex Dynamics and Vortex Methods*, Lectures in Applied Mathematics, edited by C. R. Anderson and C. Greengard (American Mathematical Society, 1991), Vol. 28, pp. 131–152.
[43]M. P. Escudier, "Observations of the flow produced in a cylindrical container by a rotating end wall," Exp. Fluids **2**, 189 (1984).
[44]A. Y. Gelfgat, P. Z. Bar-Yoseph, and A. Solan, "Three-dimensional instability of axisymmetric flow in a rotating lid-cylinder enclosure," J. Fluid Mech. **438**, 363 (2001).
[45]D. J. Tritton, *Physical Fluid Dynamics*, 2nd ed. (Clarendon, Oxford, 1988).
[46]J. Leypoldt, H. C. Kuhlmann, and H. J. Rath, "Three-dimensional numerical simulation of thermocapillary flows in cylindrical liquid bridges," J. Fluid Mech. **414**, 285 (2000).
[47]K. Boronska and L. Tuckerman, "Standing and travelling waves in cylindrical Rayleigh-Bénard convection," J. Fluid Mech. **559**, 279 (2006).
[48]C. Nienhüser and H. C. Kuhlmann, "Stability of thermocapillary flows in non-cylindrical liquid bridges," J. Fluid Mech. **458**, 35 (2002) (see also the Corrigendum, J. Fluid Mech. **480**, 333 (2003).
[49]M. Levenstam and G. Amberg, "Hydrodynamical instabilities of thermocapillary flow in a half-zone," J. Fluid Mech. **297**, 357 (1995).
[50]G. Ratnieks, A. Muiznieks, A. Mühlbauer, and G. Raming, "Numerical 3D study of FZ growth: Dependence on growth parameters and melt instability," J. Cryst. Growth **230**, 48 (2001).
[51]M. C. Navarro, L. M. Witkowski, L. S. Tuckerman, and P. Le Quéré, "Building a reduced model for nonlinear dynamics in Rayleigh-Bénard convection with counter-rotating disks," Phys. Rev. E **81**, 036323 (2010).
[52]P. Dold, A. Cröll, and K. W. Benz, "Floating-zone growth of silicon in magnetic fields I. Weak static axial fields," J. Cryst. Growth **183**, 545 (1998).
[53]K. Takagi, M. Otaka, H. Natsui, T. Arai, S. Yoda, Z. Yuan, K. Mukai, S. Yasuhiro, and N. Imaishi, "Experimental study on transition to oscillatory thermocapillary flow in a low Prandtl number liquid bridge," J. Cryst. Growth **233**, 399 (2001).
[54]V. Shevtsova, "Thermal convection in liquid bridges with curved free surfaces: Benchmark of numerical solutions," J. Cryst. Growth **280**, 632 (2005).
[55]A. Y. Gelfgat, "Three-dimensional instability of axisymmetric flows: Solution of benchmark problems by a low-order finite volume method," Int. J. Numer. Methods Fluids **54**, 269 (2007).